Journal of CO2 Utilization 58 (2022) 101922

Contents lists available at ScienceDirect

Journal of CO2 Utilization

journal homepage: www.elsevier.com/locate/jcou

Tuning basicity of dual function materials widens operation temperature window for efficient CO_2 adsorption and hydrogenation to CH_4

Alejandro Bermejo-López, Beñat Pereda-Ayo, Jon A. Onrubia-Calvo, José A. González-Marcos, Juan R. González-Velasco *

Department of Chemical Engineering, Faculty of Science and Technology, Universidad del País Vasco UPV/EHU, Barrio Sarriena, s/n, Leioa, Bizkaia 48940, Spain

ARTICLE INFO

Keywords:
CO_2 hydrogenation
Integrated CO_2 capture and utilization
Methanation
Dual function material
Tuning basicity

ABSTRACT

Mitigation of CO_2 emissions by integrated CO_2 capture and utilization (ICCU) is challenging. This work focuses on widening operation temperature window of the hydrogenation of adsorbed CO_2 to CH_4. For this, a set of dual function materials (DFMs) 4%Ru-x%Na_2CO_3-y%CaO/γ-Al_2O_3 are prepared. DFMs are deeply characterized by N_2 adsorption-desorption, XRD, H_2 chemisorption, TEM, H_2-TPR and CO_2-TPD. The catalytic behavior, in cycles of CO_2 adsorption and hydrogenation to CH_4, is evaluated and the temporal evolution of the concentration of reactants and products is analyzed. The presence of both adsorbents in the DFMs improves ruthenium dispersion and the basicity is modulated with the Na_2CO_3/CaO ratio. Ru-8Na/8Ca improves methane production over the whole temperature window compared to DFMs based only on a unique adsorbent. The best results are assigned to the promotion of contact between the carbonates of medium strength with the metallic sites, which boost the CO_2 adsorption and hydrogenation to CH_4.

1. Introduction

The significant increase of CO_2 concentration in the atmosphere, from 280 ppm in 1760 to 410 ppm in 2020 [1], has become a serious global warming problem, resulting in a series of severe climate and environmental changes [2]. The emissions of CO_2 are mainly attributed to fossil fuel consumption [3]; in particular, the power generation sector is responsible of most CO_2 emissions, followed by industrial and transportation vehicles [4]. At this point, the reduction of CO_2 emissions into the atmosphere is essential.

CO_2 capture technologies provide a key pathway to reducing CO_2 emissions, especially considering that fossil fuels will continue to play an important role in supplying global energy demand during the energy transition [5]. CO_2 capture and storage (CCS) and direct air capture (DAC) are among those technologies. Reducing CO_2 emissions, especially for CO_2 intensive industries, would be impossible at short-term without CCS technology. However, the widespread deployment of these technologies will require significant costs reduction and performance improvements.

In recent years, increasing studies have been carried out on CO_2 capture and utilization (CCU). After sequestration, CO_2 is co-feed in the synthesis of value-added products, such as methane, ethane, propane, syngas or liquid chemicals [1,6,7]. More recently, the integrated CO_2 capture and utilization technology has been proposed (ICCU), which reduces the cost of the overall process by eliminating transportation and storage of CO_2 [8]. ICCU achieves in situ CO_2 adsorption and conversion using dual function materials (DFMs), which consist of CO_2 adsorbent and catalytic phases. First, DFMs capture CO_2 from flue gas (4–14 vol% CO_2) to effectively reduce carbon emissions. When the carbon capture process is completed, the feed gas is switched to a reducing renewable agent for the conversion of the adsorbed CO_2 to synthetic fuels.

Depending on the reducing agent, the composition of the DFM and the operating conditions, the adsorbed CO_2 can be transformed into syngas or methane [9]. The transformation into syngas can take place by dry reforming of methane (ICCU-DRM) [10,11] or by reverse water gas shift (ICCU-RWGS) [12,13]. On the other hand, the transformation into methane (Eq. 1) occurs by the total hydrogenation of CO_2 (ICCU-methanation) [14–16]. If the conversion of the captured CO_2 is carried out using hydrogen from renewable energies by means of electrolysis of water, it would also be an effective solution to store excess electrical energy in chemical products. Therefore, ICCU-methanation technology is a sustainable technology approaching a closed carbon cycle without net CO_2 emissions to the atmosphere. Besides, ICCU can address the problem of intrinsic intermittency of renewable sources [17].

* Corresponding author.
E-mail address: juanra.gonzalezvelasco@ehu.eus (J.R. González-Velasco).

https://doi.org/10.1016/j.jcou.2022.101922
Received 28 January 2022; Accepted 1 February 2022
Available online 12 February 2022

$$CO_2 + 4H_2 \leftrightarrows CH_4 + 2H_2O \quad (1)$$

The first ICCU-methanation work was published in 2015 [18] and since then, the number of publications is growing exponentially [9, 19–21]. DFMs are commonly based on an alkaline or alkaline-earth compound, such as Na [22,23], Ca [18,24], Mg [16,25] or K [16,26]. Those elements are used as CO_2 adsorbents, due to the affinity of acid CO_2 to bound to a basic element and form the corresponding carbonate. On the other hand, Ru [22,27], Ni [26,28] or Rh [29] are used as catalyst due to their ability to assist the CO_2 hydrogenation to CH_4. Both phases are supported on a high surface area carrier, being γ-Al_2O_3 the most widely used. Arellano-Treviño et al. [30] studied different candidates as carrier materials for the DFM application: CeO_2 (high and low surface area), Na-Zeolite-X, H-Mordenite Zeolite, SiC, SiO_2 and mixed oxides (CeO_2-ZrO_2, ZrO_2-Y_2O_3) which could enhance the operation; although they concluded that γ-Al_2O_3 achieved the most promising results among them. Some non-supported catalysts have been recently proposed [31].

In previous works [22,24,28], it has been concluded that the presence of Ca-based compounds as adsorbent provides sites with high basicity strength into the DFM and therefore the CH_4 formation is favored at high temperatures. On the other hand, the presence of Na-based compounds, as adsorbent, leads to the appearance of medium strength basic sites and therefore the CH_4 formation is favored at intermediate operating temperatures.

On the other hand, recently Al-Mamoori et al. [32] studied the development of Ca-based adsorbents doped with Na and K. The authors concluded that the addition of K and Na improved the performance of CaO since these materials presented high CO_2 adsorption capacity, fast kinetics, and good stability above 300 °C. Lee et al. [33] performed a comparative study of adsorption and regeneration kinetics of conventional and Na_2CO_3-doped CaO-adsorbents. In this study, the authors concluded that the addition of sodium carbonate into calcium adsorbent can improve the cyclic stability of CO_2 adsorption with fast kinetics.

In this work, the joint presence of Na and Ca in Ru-based DFMs is studied, which to our knowledge has not been published to date. It is analyzed whether it is possible to modulate the basicity of a DFM and enhance the CH_4 production in an extended temperature range by varying the Na_2CO_3/CaO ratio for a total adsorbent content of 16%. For this, a set of DFMs 4%Ru-x%Na_2CO_3-y%CaO/γ-Al_2O_3 (x/y = 16/0, 12/4, 8/8, 4/12 and 0/16) are prepared by the wetness impregnation method. DFMs are widely characterized and their behavior is evaluated in cycles of CO_2 adsorption and hydrogenation to CH_4.

2. Experimental

2.1. Catalyst preparation

All samples were prepared by wetness impregnation. First, appropriated amount of $Ca(NO_3)_2{\cdot}4H_2O$ (*Merck*) and/or Na_2CO_3 (*Riedel de-Haën*) was impregnated over γ-Al_2O_3 (*Saint Gobain*). The impregnated powder was dried at 120 °C overnight and then calcined at 400 °C for 4 h (1 °C min^{-1}). Afterwards, $Ru(NO)(NO_3)_2$ (*Sigma Aldrich*) was impregnated over x%Na_2CO_3-y%CaO/γ-Al_2O_3 (x/y = 16/0, 12/4, 8/8, 4/12 and 0/16). After drying at 120 °C, the samples were stabilized by calcining again at 400 °C for 4 h (1 °C min^{-1}). The nominal loading of ruthenium was 4%.

2.2. X ray diffraction (XRD)

X-ray diffraction spectra were obtained in a *Philips PW1710* diffractometer. The samples were finely ground and were subjected to Cu Kα radiation in a continuous scan mode from 5° to 70° 2θ with 0.02 per second sampling interval.

2.3. N_2 adsorption-desorption

The N_2 adsorption-desorption analysis were carried out at the nitrogen boiling temperature (−196 °C) using an automated gas adsorption analyser (*TriStar II, Micromeritics*). The samples were pre-purged with nitrogen for 10 h at 300 °C using *SmartPrep degas system* (*Micromeritics*).

2.4. H_2 chemisorption

Ruthenium dispersion was determined using the H_2 chemisorption method in a *Micromeritics ASAP 2020* equipment. Prior to the experiments, the samples (0.2 g) were reduced with pure H_2 for 2 h at 400 °C. After that, the samples were degasified at the same temperature for 90 min. Finally, H_2 was dossed for obtaining the adsorption isotherm at 35 °C.

2.5. Transmission electron microscopy (TEM)

The morphology of the samples was analysed by transmission electron microscopy (TEM) in a *JEM-1400 Plus* instrument using a voltage of 100 kV. The reduced samples were dispersed in distillated water ultrasonically, and the solutions were then dropped on copper grids coated with lacey carbon film. In addition, STEM measurements were carried out at FEI *Titan Cubed G2 60–300* electron microscope at 200 kV. The instrument is equipped with a high-brightness *X-FEG Schottky* field emission electron gun, a monochromator, *CEOS GmbH* spherical aberration (Cs) corrector on the image side and a *Super-X* EDX system under high annular dark field (HAADF) detector for Z contrast imaging in STEM conditions (camera length of 185 mm). The nominal size of the electron probe used for STEM and EDX maps was 0.5 nm and the probe current 170 pÅ and the semiconvergence angle was 14 mrad. High-angle annular dark-field HAADF STEM images were collected with an inner detector radius of 63.5 mrad. The DFM were dispersed in ethanol ultrasonically, and the solutions were then dropped on copper grids coated with lacey carbon film.

2.6. Temperature-programmed reduction (H_2-TPR)

The reducibility of the samples was investigated by temperature programmed reduction (H_2-TPR) in a *Micromeritics AutoChem II* equipment. The samples (0.1 g) was loaded in a quartz tube reactor and pretreated at 350 °C for 15 min under 5% O_2/He (30 ml min^{-1}) and then cooled down to 35 °C. The reducing gas flow was 30 ml min^{-1} of 5% H_2/Ar and the temperature was increased from 30 °C to 950 °C with a heating rate of 10 °C min^{-1}. The water formed during reduction was trapped using a cold trap and the hydrogen consumption was continuously monitored with a TCD detector.

2.7. Temperature-programmed desorption (CO_2-TPD)

The CO_2-TPD experiments were carried out in a *Micromeritics AutoChem II* equipment. The samples (0.1 g) were pretreated at 400 °C under 5% H_2/Ar (50 ml min^{-1}) for the complete reduction of the samples before the experiment and then cooled down to 50 °C. Then, the samples were exposed to a gas stream composed of 5% CO_2/He (50 ml min^{-1}) for 1 h at RT to saturate the catalyst with CO_2. Subsequently, the samples were exposed to He (50 ml min^{-1}) for 90 min to remove the physically adsorbed CO_2 and finally they were heated from RT to 1000 °C at 10 °C min^{-1} and the CO_2 released was measured by mass spectrometry (*HIDEN ANALYTICAL HPR-20 EGA*).

2.8. . Reaction tests

Cycles of CO_2 adsorption and hydrogenation to CH_4 were carried out in a down-flow stainless steel reactor. In each activity test, 1 g of DFM

was loaded with a particle size between 0.3 and 0.5 mm. The operating temperature was measured through a thermocouple placed in the centre of the catalytic bed. Prior to the analysis, the DFMs were reduced with a stream composed of 10% H_2/Ar, progressively increasing the temperature from room temperature to 400 °C, and finally the temperature was maintained for 1 h. Then the DFM was cooled to 280 °C and the reaction temperature was varied between 280 and 400 °C, with intervals of 30 °C. In the adsorption (storage) period, a stream composed of 10% CO_2/Ar was fed for 1 min, followed by a purge with Ar for 2 min to remove weakly adsorbed CO_2 and prevent the streams from mixing. Next, in the hydrogenation (methanation) period, a stream composed of 10% H_2/Ar was fed for 2 min, followed by a purge with Ar for 1 min before starting the adsorption period again. Several isothermal cycles have been carried out at each temperature until cycle-to-cycle steady state is reached. Throughout the entire experiment, the total flow rate was set at 1200 ml min^{-1}. This flow corresponds to a space velocity of 45,000 h^{-1}. The flue gas composition was continuously monitored for quantitative analysis of CO_2, CH_4, CO and H_2O with a *MultiGas 2030 FT-IR* analyser.

The amount of CO_2 stored was calculated from Eq. (2). For that, the amount that leaves the reactor was subtracted from the amount fed. To determine the amount of CO_2 fed, the stream from the feed system was led directly to the analyser. This profile corresponds to the actual CO_2 input that was fed to the reactor.

$$STO.CO2\left(\mu mol\ g^{-1}\right) = \frac{1}{W}\int_0^t \left[F^{in}_{CO_2}(t) - F^{out}_{CO_2}(t)\right] dt \quad (2)$$

On the other hand, the CH_4, CO and H_2O productions were calculated from the following expressions:

$$Y_{CH_4}\left(\mu mol\ g^{-1}\right) = \frac{1}{W}\int_0^t F^{out}_{CH_4}(t)dt \quad (3)$$

$$Y_{CO}\left(\mu mol\ g^{-1}\right) = \frac{1}{W}\int_0^t F^{out}_{CO}(t)dt \quad (4)$$

$$Y_{H_2O}\left(\mu mol\ g^{-1}\right) = \frac{1}{W}\int_0^t F^{out}_{H_2O}(t)dt \quad (5)$$

CH_4 selectivity is determined by relating the CH_4 and CO productions since they were the only carbon based products that were detected:

$$S_{CH4}(\%) = \frac{Y_{CH_4}}{Y_{CH_4} + Y_{CO}} \times 100 \quad (6)$$

Finally, the carbon balance check was carried out from the following expression:

$$s_{CB}(\%) = \left(\frac{Y_{CH_4} + Y_{CO}}{STO.CO2} - 1\right) \times 100 \quad (7)$$

3. Results and discussion

3.1. Textural properties and phase identification

Table 1 lists the complete formulation of the samples prepared in this work and the nomenclature used to refer them. In addition, it summarizes the values of specific surface area (S_{BET}), pore diameter (d_p) and pore volume (V_p) of both the calcined and reduced samples. The γ-Al_2O_3 used has a specific surface area of 218 $m^2\ g^{-1}$ and with the incorporation of 4% ruthenium the surface area is reduced to 204 $m^2\ g^{-1}$. This reduction is mainly due to the decrease in mesoporous solid content (γ-Al_2O_3). On the other hand, when 4% ruthenium and 16% adsorbent are incorporated, either Na_2CO_3, CaO or a combination of both, the surface area is reduced to 105–113 $m^2\ g^{-1}$. The contribution of alumina to the surface area of fully formulated DFMs would be 175 $m^2\ g^{-1}$ depending on its composition (80% γ-Al_2O_3 by weight), therefore an additional phenomenon is evidenced that decreases the specific surface area. This additional decrease is assigned to the blocking of the smaller pores by the presence of the adsorbent phase or phases.

Table 1
Nomenclature and textural properties of the calcined and reduced samples.

Sample	Nomenclature	S_{BET}, $m^2\ g^{-1}$	d_p, Å	V_p, $cm^3\ g^{-1}$	S_{BET}, $m^2\ g^{-1}$	d_p, Å	V_p, $cm^3\ g^{-1}$
		calcined samples			reduced samples		
γ-Al_2O_3	Al_2O_3	218	107	0.604	–	–	–
4%Ru/γ-Al_2O_3	Ru-ref	204	104	0.546	199	108	0.549
4%Ru-16% Na/γ-Al_2O_3	Ru-16Na	105	126	0.341	128	135	0.444
4%Ru-12% Na-4% Ca/γ-Al_2O_3	Ru-12Na/4Ca	113	123	0.359	125	130	0.416
4%Ru-8%Na-8%Ca/γ-Al_2O_3	Ru-8Na/8Ca	111	118	0.336	131	130	0.439
4%Ru-4%Na-12% Ca/γ-Al_2O_3	Ru-4Na/12Ca	113	112	0.326	122	131	0.412
4%Ru-16% Ca/γ-Al_2O_3	Ru-16Ca	109	108	0.304	122	121	0.382

On the other hand, if the values of the calcined samples are compared with the reduced samples, it can be seen that the reference sample only with ruthenium (Ru-ref) slightly reduces its specific surface area after the reduction pretreatment. However, for the DFMs the surface areas increase to 122–131 $m^2\ g^{-1}$. As will be explained later by XRD, peaks belonging to nitrogenous compounds are detected in the calcined samples, which disappear after the reduction pretreatment. Therefore, the increase in surface area is assigned to the removal of residual nitrates from the DFMs. In agreement with these results, previous works [22,24] have detected the presence of nitrogenous compounds in the exhaust gases of the H_2-TPR experiments for similar DFMs.

The adsorption and desorption isotherms of N_2 at − 196 °C for the calcined and reduced samples are type IV according to the IUPAC classification, which corresponds to mesoporous solids. The isotherms present a hysteresis cycle H1 that indicates the presence of regular pores in shape and size. Representatively, Fig. S1a shows the isotherms of the calcined and reduced Ru-8Na/8Ca DFM. If the isotherms are compared to each other, it can be seen how the reduced DFM adsorbs a higher volume of N_2 irrespective the relative pressure. Consequently, the exposed surface area calculated by the BET method is higher for the reduced sample (118 $m^2\ g^{-1}$) than for the non-reduced or simply calcined one (111 $m^2\ g^{-1}$).

Alumina has a pore diameter of 107 Å and a pore volume of 0.604 $cm^3\ g^{-1}$. With the addition of the adsorbent phases together with the metal, the pore diameter increases and the pore volume is reduced. This phenomenon confirms the blocking of the smaller pores due to the presence of the adsorbent phase or phases. On the other hand, if the values of the calcined samples and the reduced samples are compared, it can be seen how after the reduction pretreatment, both d_p and V_p increase. This again confirms the presence of residual nitrates that after the calcination step are partially or totally blocking some pores of the alumina and that are eliminated after the reduction pretreatment.

The pore size distribution of the calcined and reduced samples has a unimodal distribution centered at 80–120 Å. Representatively, Fig. S1b shows the pore size distribution of the calcined and reduced Ru-8Na/8Ca DFM. The reduction pretreatment shifts the distribution towards

higher values which, is assigned to the elimination of the residual nitrates that are partially blocking the pores. On the other hand, the area under the curve increases in the reduced DFM, indicating a greater pore volume, as observed in Table 1.

Fig. 1a shows the X-ray diffraction spectra of the alumina, the reference sample only with ruthenium (Ru-ref) and the calcined DFMs. Alumina exhibits a diffraction profile with low intensity broad peaks characteristic of an amorphous solid. With the addition of 4% Ru (Ru-ref), three intense peaks appear at 28.0, 35.1 and 54.2° 2θ, assignable to RuO_2. On the other hand, with the joint addition of the metal and the adsorbent phase or phases, the three peaks corresponding to RuO_2 are also detected, however, additional peaks appear. In the DFM Ru-16Ca, new peaks are detected at 11.1 and 18.9° 2θ belonging to $Ca_6Al_2O_6(NO_3)_6{\cdot}xH_2O$ and in all DFMs with sodium an additional peak appears at 31.9° 2θ belonging to $NaNO_3$.

The X-ray diffraction spectra of the alumina, the reference sample only with ruthenium (Ru-ref) and the DFMs after the reduction pretreatment are shown in Fig. 1b. In the spectrum of the Ru-ref sample, the peaks belonging to RuO_2 disappear and only a low intensity peak belonging to metallic ruthenium was detected at 44.0° 2θ. Cimino et al. [27] for a reduced $Ru/\gamma\text{-}Al_2O_3$ catalyst also observed a similar behavior. In the DFMs the peaks belonging to RuO_2 also disappear and the peak corresponding to metallic ruthenium is detected. On the other hand, the peaks belonging to nitrogenous species disappear and no additional peaks belonging to the adsorbents are distinguished. Therefore, based on the XRD spectra it is suggested that the reduction pretreatment is adequate to reduce the ruthenium and decompose the residual nitrates.

3.2. Ruthenium dispersion

The ruthenium dispersion of the samples is determined by H_2 chemisorption considering a stoichiometry H/Ru = 1 [34]. Table 2 shows the dispersion values (D_m) of the reference sample only with ruthenium (Ru-ref) and the prepared DFMs. The Ru-ref sample has a dispersion of 11.5%, and in general, the dispersion increases with the addition of the adsorbent to 19.6–24.8% with the exception of the DFM Ru-16Ca, which presents a value of 9.8%. In own previous work [22], we studied the effect of the adsorbent loading on DFMs based on ruthenium and on CaO or Na_2CO_3 as adsorbents. We concluded that the presence of CaO penalizes the dispersion of ruthenium while the presence of Na_2CO_3 promotes it. Therefore, based on H_2 chemisorption results, in addition to concluding that the presence of Na_2CO_3 promotes dispersion, this promotion increased by the joint presence of both adsorbents. Note that the highest dispersion values are presented by DFMs based on sodium and calcium together. Specifically, the highest dispersion value (24.8%) is presented by the DFM Ru-8Na/8Ca.

Table 2
Ru dispersion and particle size estimated from H_2 chemisorption, TEM micrographs and XRD spectra.

Sample	D_m, %	d_c (Ru-H_2), nm	d_c (Ru-TEM), nm	d_c (Ru-XRD), nm
Ru-ref	11.5	11.6	9.5	13.8
Ru-16Na	19.6	6.8	8.7	9.0
Ru-12Na/4Ca	21.1	6.3	7.8	–
Ru-8Na/8Ca	24.8	5.4	6.4	–
Ru-4Na/12Ca	20.4	6.5	7.0	–
Ru-16Ca	9.8	13.6	10.0	11.3

From the dispersion values, an average particle size is estimated considering spherical particles. Logically, the smallest particles are shown by the DFMs based on both adsorbents and the DFM Ru-8Na/8Ca presents the smallest size of 5.4 nm.

Fig. 2 shows the TEM micrographs of the reference sample only with ruthenium (Ru-ref) and the prepared DFMs. The darkest circular areas correspond to ruthenium particles due to the higher atomic number of Ru with respect to other elements in the DFM. Clearly, for the Ru-ref sample and for the DFM Ru-16Ca, larger particles are observed compared to the DFMs that present sodium in their composition. However, for the rest of the DFMs, no significant differences are observed between them in the micrographs. At this point, in order to make a more exhaustive comparison, an average particle size is estimated by TEM. For this, the particles are considered to have a circular shape and at least 100 particles were counted for each sample and the estimated values are

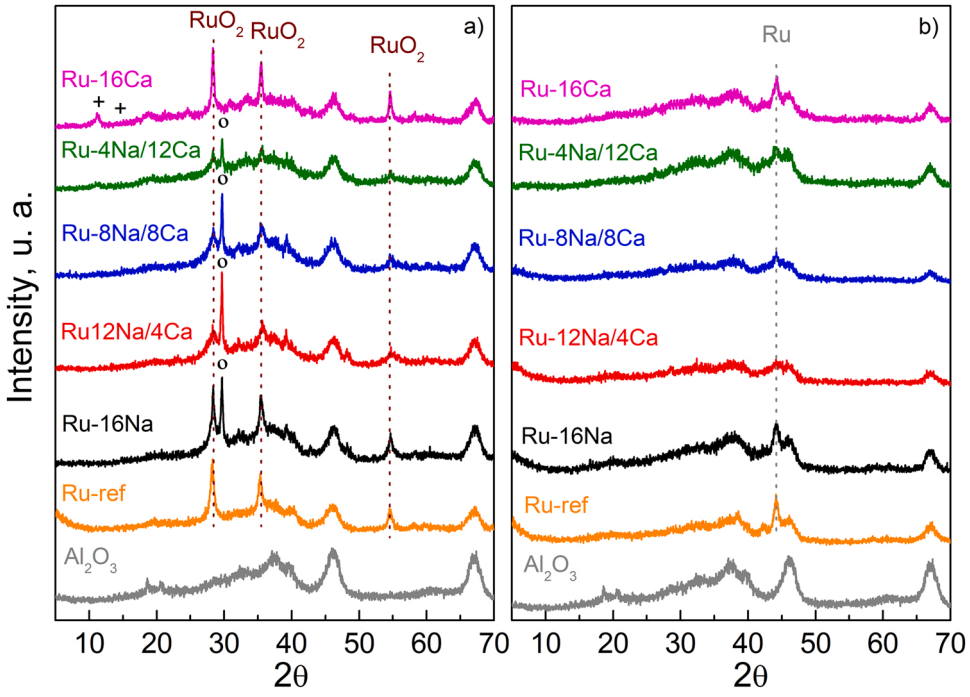

Fig. 1. XRD diffraction spectra of the alumina, the reference sample only with ruthenium (Ru-ref) and of the DFMs after calcination (a) and after the reduction pretreatment (b). Diffraction peaks belonging to $Ca_6Al_2O_6(NO_3)_6{\cdot}xH_2O$ are identified with (+) and belonging to $NaNO_3$ with (o).

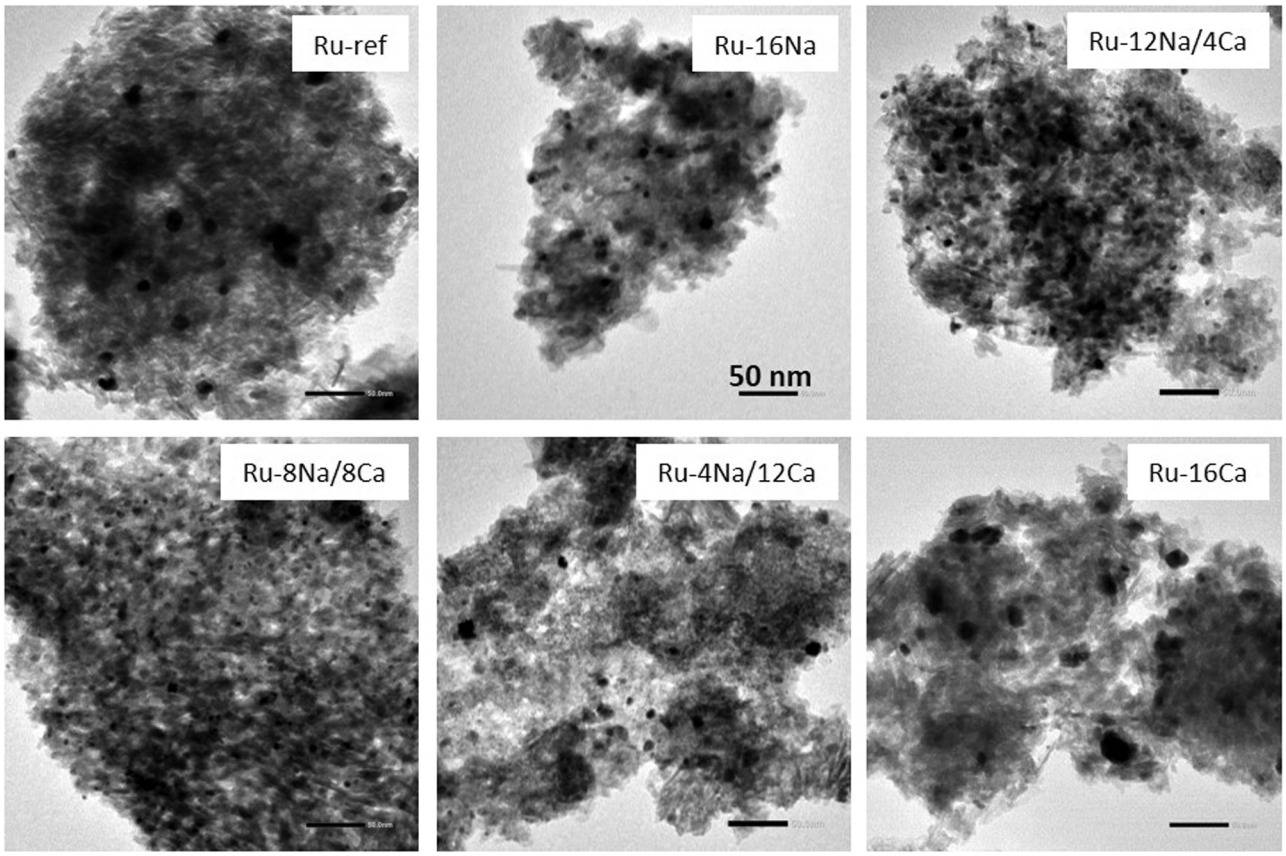

Fig. 2. TEM micrographs of the reference sample only with ruthenium (Ru-ref) and of the DFMs with different Na_2CO_3/CaO ratios.

shown in Table 2. It is confirmed that the DFMs based on Na_2CO_3 have lower sizes and more specifically those based on both adsorbents. Furthermore, again the lowest value (6.4 nm) is presented by the DFM Ru-8Na/8Ca.

Fig. 3 shows a HAADF image and EDX maps for Al, Na, Ca and Ru for reduced DFM Ru-8Na/8Ca. It is observed how both adsorbents (Na and Ca) are homogeneously distributed over the alumina surface. However, ruthenium is in the form of spherical particles as seen in TEM images (Fig. 2). Additionally, the average particle size of Ru is determined from the EDX map (Fig. 3e) and a value of 5.5 nm is obtained, similar to that obtained by TEM images (6.4 nm) and by H_2 chemisorption (5.4 nm).

Finally, a crystal size is also estimated from the ruthenium peak (44.0° 2θ) of the diffraction profiles of Fig. 1b and is summarized in Table 2. This size can only be estimated for the sample Ru-ref and for DFMs based solely on calcium or sodium, since for DFMs based on both adsorbents the peak is not well defined. In general, similar trends are obtained by the three techniques used, so it is concluded that the presence of sodium promotes the dispersion of ruthenium and this promotion is greater when both adsorbents are present.

3.3. Programmed temperature techniques (H_2-TPR and CO_2-TPD)

The reducibility of the samples is evaluated by temperature programmed reduction with H_2. Fig. 4 shows the H_2 consumption profiles in the H_2-TPR experiments of the reference sample only with ruthenium (Ru-ref) and the prepared DFMs. The Ru-ref sample shows a hydrogen consumption centered at 100 °C, which is assigned to the reduction of RuO_2, in line with the observed by XRD. This assignment was confirmed by the H_2/Ru ratio determined which is close to 2. With the incorporation of the adsorbent phase or phases, H_2 consumption shifts to higher temperatures and increases significantly. The H_2/Ru ratio is between 12 and 15 for the five DFMs studied. This value is much higher than the value of 2 obtained by the reference sample. Therefore, an additional phenomenon that is consuming H_2 is evidenced.

In order to collect more information and clarify the H_2 consumption patterns, the exhaust gas from the H_2-TPR experiments was analysed by mass spectrometry, as we already did in our previous works [22,24]. As an example, Figure S2 shows the evolution of NO, NH_3 and CH_4 during a H_2-TPR performed up to 400 °C with an isothermal step of 1 h for the

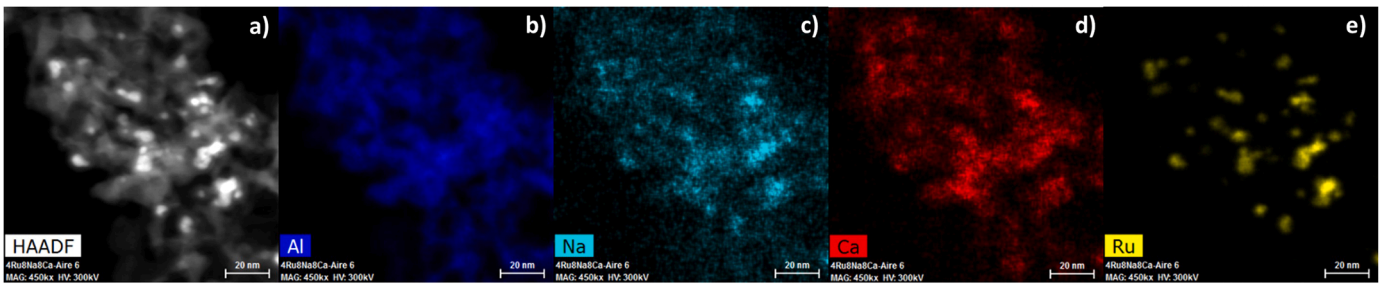

Fig. 3. STEM image (a) and EDX maps for Al (b), Na (c), Ca (d) and Ru (e) for reduced DFM Ru-8Na/8Ca.

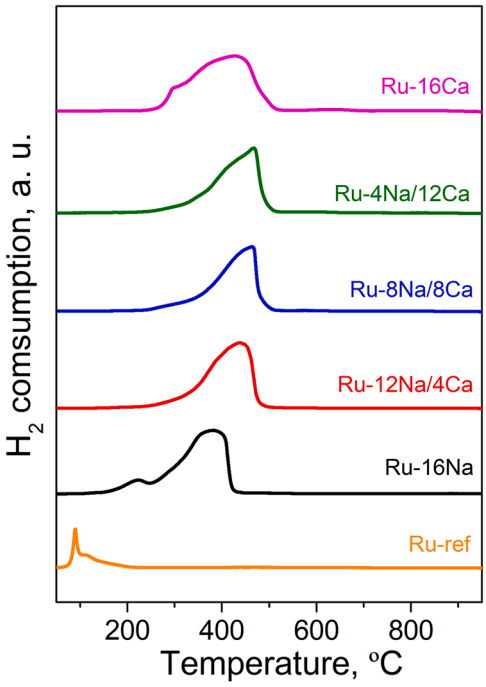

Fig. 4. H_2-TPR patterns for the DFMs with different Na_2CO_3/CaO ratios. Ru-ref sample is also included as reference.

Ru-8Na/8Ca DFM. Nitrogen monoxide (NO) is the first product detected. The NO formation is related to the decomposition of residual nitrates belonging to the adsorbent and noble metal precursors that have not been completely decomposed during the calcination step.

The onset of NH_3 formation is detected at higher temperatures. The NH_3 formation requires the noble metal in its metallic state, and therefore the NH_3 formation can be used as an indirect way to determine the temperature at which ruthenium begins to reduce. On the other hand, the CH_4 formation is attributed to the hydrogenation of the CO_2 adsorbed in the samples, due to exposure to the environment before the experiment. The CH_4 formation by hydrogenation of CO_2 requires the presence of metallic ruthenium. Therefore, the starting temperature for the detection of CH_4 coincides with that of NH_3.

As a conclusion, the increase of the H_2 consumption for the prepared DFMs (with respect to the Ru-ref sample) can be unequivocally attributed to the reduction of residual nitrates and the hydrogenation of carbonates. Furthermore, the presence of residual nitrates delays the reduction of ruthenium. As can be seen in Figure S2, NO is detected first and then NH_3. Since the start of NH_3 production is consistent with the start of ruthenium reduction, it suggest that the presence of residual nitrates is delaying the reduction of ruthenium. This was confirmed with an additional H_2-TPR/O_2-TPO/H_2-TPR experiment (not shown). The absence of nitrates in the second H_2-TPR and the shift to lower temperatures from the first to the second H_2-TPR confirms that the presence of nitrates delays the reduction of ruthenium.

Likewise, additional experiments are carried out by performing an isothermal step at 400 °C for one hour. Figure S3 shows the H_2 consumption during these experiments. No H_2 consumption above 400 °C is detected. These results demonstrates that ruthenium is completely reduced, confirming that the reduction pretreatment chosen prior to the activity tests is adequate.

The basicity of the samples is evaluated by temperature programmed desorption of CO_2 (CO_2-TPD). Fig. 5a shows the evolution of the CO_2 signal measured by a mass spectrometer (m/e = 44) as a function of temperature for alumina, the reference sample only with ruthenium (Ru-ref) and the prepared DFMs. Alumina exhibits a small desorption peak at low temperature. The incorporation of 4% ruthenium (Ru-ref) does not

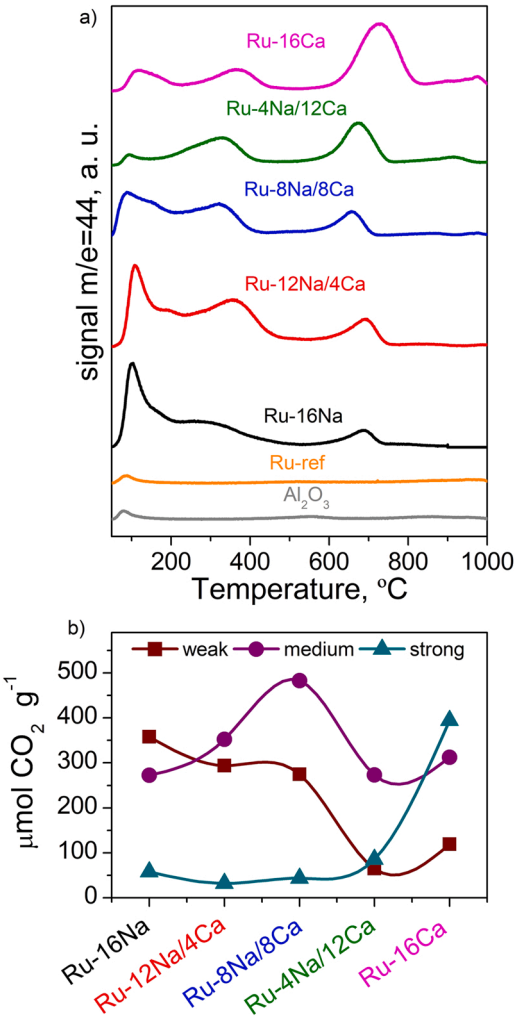

Fig. 5. (a) CO_2-TPD patterns for the DFMs with different Na_2CO_3/CaO ratios. Al_2O_3 and Ru-ref samples is also included as reference. (b) Evolution of the weak, medium and strong basicity in µmol of CO_2 g^{-1} for the DFMs with different Na_2CO_3/CaO ratios.

modify the profile, also obtaining only a small desorption peak at low temperature. Porta et al. [15] also did not observe a modification of the desorption profile with the incorporation of Ru into alumina. This peak is assigned to the decomposition of bicarbonates that result from the interaction between CO_2 and the surface hydroxyl groups of alumina [35,36].

The incorporation of an adsorbent phase or phases significantly increases the amount of CO_2 desorbed (Fig. 5a). At this point, depending on the desorption temperature, weak, medium and strong basicity sites are distinguished. Weak basic sites are unstable and easily decomposed below 250 °C. The medium basic sites are decomposed between 250 and 700 °C while the strong basic sites are highly stable and decomposed at temperatures above 700 °C [37]. Porta et al. [16] analyzed by FTIR the nature of the CO_2 adsorbed on Ru-K/Al_2O_3 and Ru-Ba/Al_2O_3 DMs. Bands belonging to carbonates adsorbed on the adsorbent phases are only observed. The authors did not observe typical surface species of CO_2 adsorption on the alumina support, so they concluded that the adsorbent phase covers the surface of the alumina.

Fig. 5b shows the contribution in µmol g^{-1} to each type of basicity for DFMs. DFM Ru-16Na clearly has the highest weak basicity and DFM Ru-16Ca the highest strong basicity. These results are in agreement with those previously obtained, in which the presence of Na_2CO_3 promotes the weak basicity and the presence of CaO the strong basicity [22,24].

However, in DFMs based on both adsorbents, the medium basicity is predominant and, specifically, the Ru-8Na/8Ca DFM is the one with the highest medium basicity. Therefore, by adding Na_2CO_3 and CaO together, the basicity strength of DFMs can be modulated. This aspect is of special interest given that in the cyclical process of CO_2 adsorption and hydrogenation to CH_4, only the CO_2 that can be both stored and released, at a given temperature, is the one that participates in the operation.

3.4. Catalytic activity in successive cycles of CO_2 adsorption and hydrogenation to CH_4

Fig. 6 shows the evolution of the concentrations of CO_2, CH_4, H_2O and CO in a cycle of CO_2 adsorption and hydrogenation to CH_4 for the DFM Ru-8Na/8Ca operating at 400 °C. Note that the CO concentration is referred to the right ordinate axis in ppm. In addition, Fig. 6 also shows the CO_2 concentration profile fed (gray line). In the adsorption period, a stream with 10% CO_2 is fed to the reactor for 1 min, followed by a 2 min purge. The hydrogenation period then begins by admitting 10% H_2 to the reactor over 2 min and the cycle is ended with an additional 1 min purge.

In the adsorption period, the CO_2 concentration progresively increases to a value of 10%, corresponding to that of the feed. If the input CO_2 signal (red line) is compared with the output CO_2 signal (gray line), it can be seen that during the first moments of the period the adsorption is total.

At this point, it is important to take into account that the decomposition temperature of Na_2CO_3 is drastically reduced when supported on large surface materials, such as Al_2O_3. Nguyen et al. [38] observed by TGA and XRD the decomposition of the bulk Na_2CO_3 at 850 °C, while the Na_2CO_3 supported on alumina began to decompose at 135 °C. In fact, they recorded a negligible weight loss for Na_2CO_3 supported in alumina above 400 °C, revealing complete decomposition.

Therefore, whenever the decomposition of Na_2CO_3 to "Na_2O" species occurs, the adsorption of CO_2 in the sodium phase can be described as the carbonation of an alkaline earth compound [38–40]. Consequently, as the DFM is composed of both adsorbents (Na and Ca), the adsorption of CO_2 during the first moments of the period can occur through Eq. (8) and Eq. (9):

$$CaO + CO_2 \leftrightarrows CaCO_3 \quad (8)$$

$$Na_2O + CO_2 \leftrightarrows Na_2CO_3 \quad (9)$$

After that, CO_2 begins to be detected at the outlet (red line) and surprisingly the H_2O signal (blue line) increases. The presence of CO_2 in the exhaust gases indicates that the adsorption sites begin to saturate until reaching the value of the feed (10%) at 0.5 min of the adsorption period. Therefore, the 1 min duration of the adsorption period is sufficient to completely saturate the DFM. On the other hand, as water is also detected, CO_2 is also adsorbed on hydrated sites:

$$Ca(OH)_2 + CO_2 \leftrightarrows CaCO_3 + H_2O \quad (10)$$

$$2NaOH + CO_2 \leftrightarrows Na_2CO_3 + H_2O \quad (11)$$

Consequently, CO_2 adsorption can occur on the oxide sites (Eq. 8 and Eq. 9) and on the hydrated sites (Eq. 10 and Eq. 11) and since at the beginning of the period, the adsorption is total and H_2O is not detected, the oxide sites are proposed as more active for the CO_2 adsorption. In the purge, the curve belonging to the outlet CO_2 concentration (red line) presents a higher value compared to the inlet one (gray line). This fact indicates that part of the weakly adsorbed CO_2 is released during the purge. At this point, the amount of CO_2 stored is determined from Eq. (2) and results in 352 μmol g^{-1} (Table 3).

Additionally, in the adsorption period a small CO production is also detected. Note that the scale is referred to the right ordinate axis in ppms. The CO production is assigned to the partial hydrogenation of the CO_2 fed by chemisorbed hydrogen on the metal sites. The amount of CO produced and the amount of H_2O released are determined by Eq. (4) and Eq. (5) and the values are collected in Table 3.

In the hydrogenation period (Fig. 6), an instantaneous peak of CH_4 is detected, however the peak of H_2O is delayed by its adsorption on the basic sites of the adsorbent. Consequently, in this period the carbonates are decomposed by the presence of H_2 (Eq. 12 and Eq. 13), CO_2 is hydrogenated to CH_4 (Eq. 1) and part of the water remains adsorbed forming hydroxides (Eq. 14 and Eq. 15).

$$\text{Step 1a: } CaCO_3 \leftrightarrows CaO + CO_2 \quad (12)$$

$$\text{Step 1b: } Na_2CO_3 \leftrightarrows Na_2O + CO_2 \quad (13)$$

$$\text{Step 2: } CO_2 + 4H_2 \leftrightarrows CH_4 + 2H_2O \quad (1)$$

Table 3
Stored CO_2 and CH_4, CO and H_2O productions during the adsorption and hydrogenation periods for the DFM Ru-8Na/8Ca operating a 400 °C.

	CO_2 storage, μmol g^{-1}	Y_{CH4}, μmol g^{-1}	Y_{CO}, μmol g^{-1}	Y_{H2O}, μmol g^{-1}
Adsorption period	352	–	14	183
Hydrogenation period	–	357	7	556

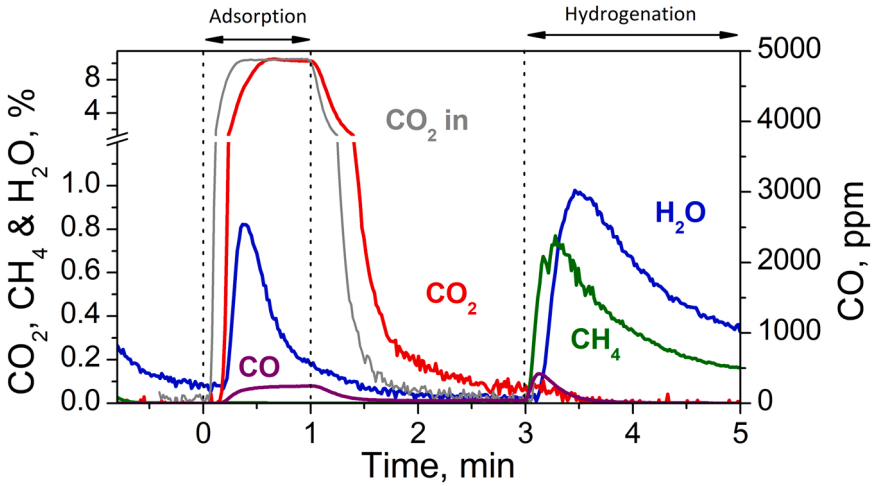

Fig. 6. CO_2, H_2O, CH_4 and CO concentration profiles during one cycle of CO_2 adsorption and hydrogenation to CH_4 for the DFM Ru-8Na/8Ca operating a 400 °C.

Step 3a: $CaO + H_2O \leftrightarrows Ca(OH)_2$ (14)

Step 3b: $Na_2O + H_2O \leftrightarrows 2NaOH$ (15)

The amounts of CH_4 and H_2O produced are obtained from Eq. (3) and Eq. (5). Furthermore, in the hydrogenation period, a small amount of CO is also produced, which is determined by Eq. (4). All values are summarized in Table 3. Finally, selectivity towards CH_4 is determined by Eq. (6) and it is 98%.

To check the reliability of the data, the error with which the carbon balance is closed is determined. For this, Eq. (7) is used and the error is around 3%. On the other hand, the total amount of water produced is related to the production of CH_4. This relationship results in 2.01, very close to the stoichiometry of the methanation reaction (Eq. 1).

It is also worth to note at this point that the CO_2 adsorption and hydrogenation is a cyclic operation. All the catalytic parameters, i.e. CO_2 adsorption, CH_4 production and CO production, are calculated once cycle-to-cycle steady state is reached. As a cyclic operation, this means that the state of the catalyst at a given point depends on the previous history. Therefore, at the end of the regeneration period some CO_2 will remain adsorbed. Consequently, at the beginning of the adsorption period some basic sites will be already occupied by CO_2. Thus, the adsorption capacity of the DFM will be somewhat limited by this fact. However, this does not affect the carbon balance. On the one hand, the amount of CO_2 stored in the DFM is calculated by Eq. (2) based on the CO_2 concentration signal experimentally recorded. In this calculation, the CO_2 already present in the sample (that strongly bonded which has not been decomposed during the hydrogenation) is not quantified. Then, CH_4 and CO formation is quantified during the subsequent hydrogenation period. On the other hand, the carbon balance relates the amount of CO_2 adsorbed during the adsorption period with respect to the amount of carbon based products (CH_4 and CO) during the hydrogenation period.

Fig. 7 shows the evolution of CH_4 and CO productions for all DFMs in the temperature range 280–400 °C. These values are obtained from evolutions similar to those in Fig. 6 and in all cases, it is possible to close the carbon balance with an error below ± 5%. CH_4 production (Fig. 7a) shows different trends depending on each DFM. The DFM Ru-16Ca shows an upward trend with the operating temperature; therefore, it presents the maximum production (336 μmol g^{-1}) at 400 °C. On the other hand, the DFM Ru-16Na hardly shows variation with temperature. This DFM produces 310 μmol g^{-1} at 310 °C, however, the production does not fall below 281 μmol g^{-1} in all the temperature range studied. These opposite tendencies are due to the different types of basicity determined in the CO_2-TPD experiments (Fig. 5a and b). In the DFM Ru-16Ca the strong basicity is predominant, thus the increase in temperature can decompose a greater quantity of CO_2 to be hydrogenated. On the other hand, the DFM Ru-16Na presents mainly weak basicity, so carbonates can decompose at significantly lower temperatures and the increase in operating temperature limits production since the stability of carbonates is reduced. Porta et al. [16] also reported a higher stability of Ca carbonates compared to Na carbonates. Efremova et al. [41,42] assigned the better catalytic activity to the enhanced basicity, which improves the adsorption and the activation of CO_2.

The DFM Ru-12Na4Ca also shows little variability in CH_4 production with operating temperature. In this occasion, the maximum production is at 340 °C and is 268 μmol g^{-1}. Although the presence of both adsorbents slightly improves the dispersion and the medium basicity is promoted, it is not possible to improve the CH_4 production with this formulation. On the other hand, the DFM Ru-4Na12Ca shows an upward trend with temperature. At 280 °C it produces 234 μmol g^{-1} and the production increases to 372 μmol g^{-1} at 400 °C. This DFM produces a higher amount of CH_4 over the entire temperature range compared to the DFM Ru-16Ca and produces a higher amount in the 340–400 °C range compared to the DFM Ru-16Na. Consequently, in a general way, the presence of both adsorbents improves CH_4 production, especially at higher operating temperatures.

Finally, the DFM Ru-8Na/8Ca notably improves the CH_4 production in the range 280–340 °C compared to the DFM Ru-4Na12Ca and the maximum production (364 μmol g^{-1}) is at 370 °C. Furthermore, the DFM Ru-8Na/8Ca exhibits superior production across the entire temperature range compared to the DFMs Ru-16Na and Ru-16Ca. At this point, the DFM Ru-8Na/8Ca is proposed as the most active for the CH_4 production in the temperature range studied. In the CO_2-TPD experiments (Fig. 5b) it has been observed that the joint incorporation of 8% Na_2CO_3 and 8% CaO significantly increases the medium basicity. Likewise, the presence of both adsorbents also improves the dispersion of ruthenium (Table 2). These improvements promote the contact between the carbonates of medium strength with the metal sites and consequently the CO_2 adsorption and hydrogenation to CH_4. Note that the maximum amount of CH_4 produced (364 μmol g^{-1}) is less than the average basicity (≈490 μmol g^{-1}, Fig. 5b). As mentioned previously, only part of the active adsorption sites are involved in the reaction.

Fig. 7b shows the evolution of CO production for all DFMs in the temperature range 280–400 °C. All DFMs show the same trend, CO production increases with operating temperature. The increase in temperature favors the RWGS and consequently a greater amount of CO is produced. Analyzing Fig. 7b clearly the DFM with only sodium (Ru-16Na) produces much amount of CO compared to the rest of DFMs. In fact, the selectivity to CH_4 at 400 °C is reduced to 92%. On the other hand, DFM Ru-16Ca presents a significantly lower CO production, showing high selectivity to CH_4 even at 400 °C (97%). Previous studies in the literature have concluded that the addition of Ca to catalysts for CO_2 methanation improves the selectivity to CH_4 by strengthening the

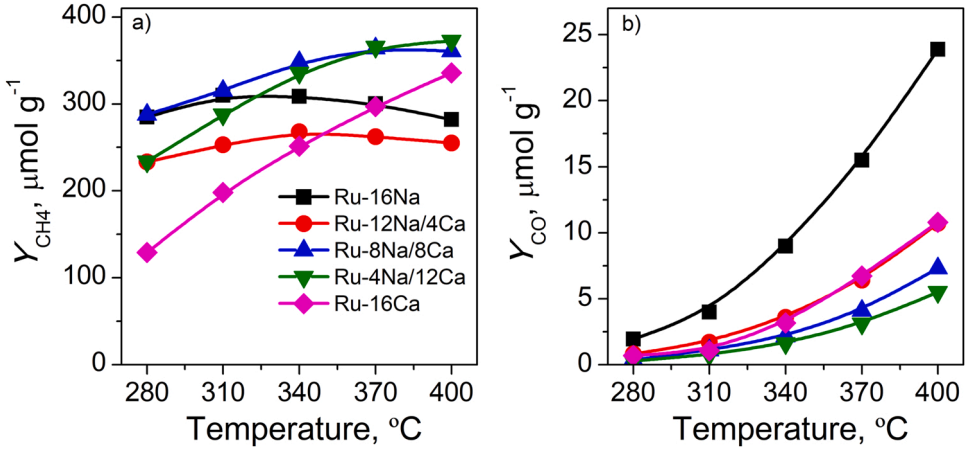

Fig. 7. Evolution of CH_4 (a) and CO (b) productions with temperature for the DFMs with different Na_2CO_3/CaO ratios.

CO_2 chemisorption, while the addition of Na favors the formation of CO [43,44].

On the other hand, it seems that the joint addition of both adsorbents further limits CO production. The Ru-8Na/8Ca as well as Ru-4Na/12Ca DFMs show a selectivity at 400 °C of 98%. The positive effect on the selectivity of the presence of Ca has a greater influence than that of Na. In addition, as dispersion is increased, more metal sites are available to promote complete hydrogenation of CO_2.

Fig. 8 shows the temporal evolutions of the CH_4 concentration during the hydrogenation period for all DFMs in the temperature range 280–400 °C. From these evolutions, the amount of CH_4 produced shown in Fig. 7a has been determined. The evolutions of the different DFMs show significant differences, especially at low operating temperatures. If the CH_4 concentration evolutions of DFMs based solely on a unique adsorbent at 280 and 310 °C are compared, the maximum CH_4 concentration is found at initial times for the Ru-16Ca DFM compared to the Ru-16Na. Therefore, this suggest that the CH_4 formation rate is faster for Ca than for Na when operating at low temperatures.

The CH_4 formation of DFMs based on both adsorbents shows fast CH_4 formation rate in which most of the formation occurs in the first minute of the hydrogenation period. Therefore, the time of the hydrogenation period could be shortened to obtain a higher conversion of the H_2 fed without drastically reducing the CH_4 production. In previous works [45,46], we modeled, simulated and optimized the CO_2 adsorption and hydrogenation to CH_4, which suggested the selection of moderate hydrogenation times because of a compromise between the H_2 conversion and CH_4 production. In this context, a fast CH_4 formation rate is crucial for the joint optimization of both parameters.

Finally, the obtained CH_4 productions are compared with those reported by other authors. Table 4 lists the CH_4 productions per gram of DFM and per cycle (Y_{CH4}) for the DFMs of this work together with other DFMs with similar formulation from the literature. CH_4 productions are in a wide range (47–1050 μmol g^{-1}). Comparison is not easy because of different operation parameters as temperature, total duration of the cycle, total flow rate and H_2 concentration in the hydrogenation period, also shown in the Table 4. Note, for example, that the duration of the cycles performed in this work is significantly lower than in other reported cycles. Nevertheless, in order to obtain comparable values, we established a new catalytic parameter as the production of CH_4 per gram of DFM and per minute (Y'_{CH4}).

It can be seen in Table 4 that Y'_{CH4} of DFMs of this study are notably higher than others in the literature, in most cases so higher as an order of magnitude. Also, note that in the cycles performed in this work, there is a purge of 2 min after adsorption and one minute after hydrogenation. Therefore, of the 6 min of a cycle duration, 50% (3 min) correspond to the purge period. Lab-scale purge has been introduced to prevent methane from being produced from non-adsorbed CO_2, but in commercial operation it could be reduced or even eliminated. This fact would lead to a substantial increase in the production of CH_4 per gram of DFM and time unit (Y'_{CH4}). The purge periods of the cycles carried out by other authors account for less than 17% of the total duration of the cycle. Therefore, it can be concluded that the DFMs of this work present a higher CH_4 production per unit of time compared to the few studies reported in the literature.

Table 4
CH_4 productions per gram of DFM and per cycle (Y_{CH4}) and per gram of DFM and per minute (P_{CH4}) together with the operational conditions of the DFMs of this study and those shown by other authors.

DFM	Y_{CH4}, μ mol g^{-1}	Y'_{CH4}, μmol g^{-1} min^{-1}	T, °C	t_{cycle}, min	Q_T, ml min^{-1}	$[H_2]$, %	Ref
4%Ru-16% Na/ Al_2O_3	310	51.7	310	6	1200	10	This work
4%Ru-12% Na-4% Ca/Al_2O_3	268	44.7	340	6	1200	10	This work
4%Ru-8% Na-8% Ca/Al_2O_3	364	60.7	370	6	1200	10	This work
4%Ru-4% Na-12% Ca/Al_2O_3	372	62.0	400	6	1200	10	This work
4%Ru-16% Ca/ γ-Al_2O_3	336	56.0	400	6	1200	10	This work
5%Ru-10% CaO/ Al_2O_3	500	3.3	320	150	26	4	[27]
5%Ru-10% Na_2CO_3/ Al_2O_3	1050	7.0	320	150	26	4	[27]
5%Ru-10% K_2CO_3/ Al_2O_3	910	6.1	320	150	26	4	[27]
5%Ru-10% Na_2CO_3/ Al_2O_3	614	7.3	320	84	200	15	[28]
1%Ru-5% K/Al_2O_3	176	7.3	350	24	100	4	[14]
1%Ru-5% Ca/Al_2O_3	107	4.5	350	24	100	4	[14]
1%Ru-16% Ba/Al_2O_3	153	6.4	350	24	100	4	[14]
1%Ru-3% Na/ Al_2O_3	47	2.0	350	24	100	4	[14]
1%Ru-5% Li/Al_2O_3	340	11.3	293	30	33	10	[25]

4. Conclusions

Ru-Na_2CO_3-CaO/Al_2O_3 DFMs with different Na_2CO_3/CaO ratios have been synthesized for the CO_2 adsorption and hydrogenation to CH_4. The addition of the metal and the adsorbent single-phase or

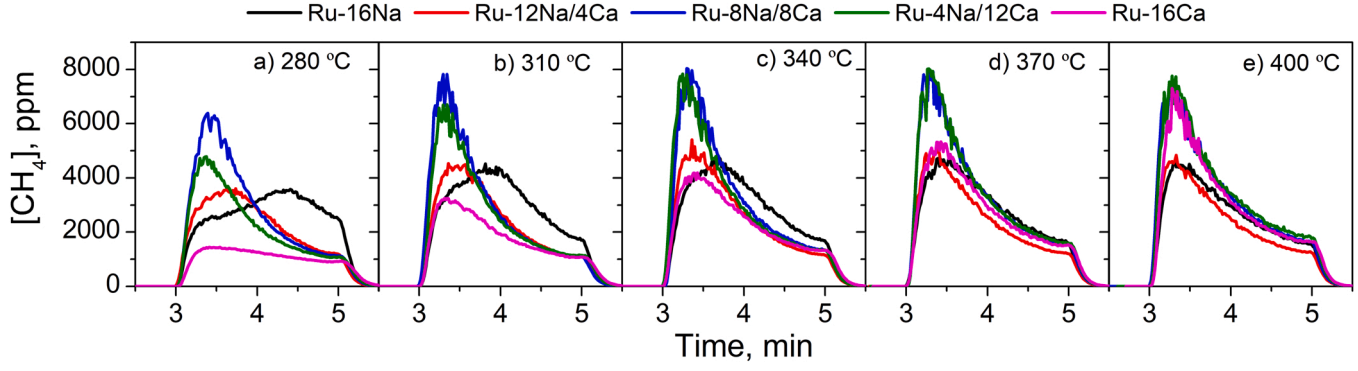

Fig. 8. CH_4 concentration profiles during the hydrogenation period at different temperatures for the DFMs with different Na_2CO_3/CaO ratios.

combined-phases reduces the surface area of the DFM by reducing the amount of mesoporous solid (alumina) and by partially or totally blocking the smaller pores. Peaks belonging to RuO_2 and nitrogenous compounds appear in the XRD spectra of the calcined samples. However, after the reduction pretreatment the nitrogenous species decompose and the ruthenium is completely reduced. Therefore, based on the results of XRD and H_2-TPR, it can be concluded that the proposed pretreatment needs to be achieve prior to activity tests.

The presence of only CaO in a DFM slightly limits the dispersion of Ru, whereas the presence of Na_2CO_3 significantly promotes it. Furthermore, the joint presence of both adsorbents boost the ruthenium dispersion. In a DFM with only sodium, weak basicity predominates, while in a DFM with only calcium strong basicity is predominant. On the other hand, by varying the Na_2CO_3/CaO ratio, it has been possible to modulate the basicity of DFM and promote the basic sites with medium strength. In this context, the DFM Ru-8Na/Ca composed of 8% of both Na_2CO_3 and CaO has the highest medium basicity.

The catalytic activity in cycles of CO_2 adsorption and hydrogenation to CH_4 presents different trends with the operating temperature according to the Na_2CO_3/CaO ratio of the DFM. The presence of Na_2CO_3 favors the CH_4 production at intermediate temperatures (310 °C), while the presence of CaO favors it production at high temperatures (400 °C), which correlates with the basicity results. However, the presence of both adsorbents, in general, boosts the production of CH_4 in the entire temperature range studied (280–400 °C). The DFM Ru-8Na/Ca, selected as optimal, produces 364 μmol g^{-1} of CH_4 at 370 °C with a selectivity of 99%. The improved ruthenium dispersion and the presence of a greater number of basic sites with medium strength boost the adsorption of CO_2 and hydrogenation to CH_4. These improvements enhance the contact between the carbonates and the metal sites, favoring a fast CH_4 formation rate. Finally, DFMs synthesized in this work present a CH_4 production per amount of DFM and per unit of time more than one order of magnitude of that reported by other authors in the literature.

CRediT authorship contribution statement

Alejandro Bermejo-López: Validation, Methodology, Investigation, Writing – original draft. **Beñat Pereda-Ayo:** Conceptualization, Methodology, Visualization, Writing – review & editing. **Jon A. Onrubia-Calvo:** Methodology, Visualization, Writing – review & editing. **José A. González- Marcos:** Methodology, Data curation, Supervision, Funding acquisition. **Juan R. González-Velasco:** Conceptualization, Supervision, Project administration, Funding acquisition.

Declaration of Competing Interest

The authors declare that they have no known competing financial interests or personal relationships that could have appeared to influence the work reported in this paper.

Acknowledgements

The financial support from the Science and Innovation Spanish Ministry (PID2019–105960RB-C21) and the Basque Government (IT1297–19) is acknowledged. The authors thank for technical and human support provided by SGIker (UPV/EHU Advanced Research Facilities/ ERDF, EU).

Appendix A. Supporting information

Supplementary data associated with this article can be found in the online version at doi:10.1016/j.jcou.2022.101922.

References

[1] W. Gao, S. Liang, R. Wang, Q. Jiang, Y. Zhang, Q. Zheng, B. Xie, C.Y. Toe, X. Zhu, J. Wang, L. Huang, Y. Gao, Z. Wang, C. Jo, Q. Wang, L. Wang, Y. Liu, B. Louis, J. Scott, A. Roger, R. Amal, H. He, S. Park, Industrial carbon dioxide capture and utilization: state of the art and future challenges, Chem. Soc. Rev. 49 (2020) 8584–8686.

[2] S. Wang, G. Li, C. Fang, Urbanization, economic growth, energy consumption, and CO_2 emissions: empirical evidence from countries with different income levels, Renew. Sustain. Energy Rev. 81 (2018) 2144–2159.

[3] B. Abirami, M. Radhakrishnan, S. Kumaran, A. Wilson, Impacts of global warming on marine microbial communities, Sci. Total Environ. 791 (2021), 147905.

[4] K. Abu-Saqer, S.H. Lubbad, Assessment of various treatment methods and reagents for cleanup and conditioning of sphagnum peat moss as sorbents in removal of malachite green as a cationic organic dye probe from water, SN Appl. Sci. 1 (2018) 20.

[5] E.I. Koytsoumpa, D. Magiri – Skouloudi, S. Karellas, E. Kakaras, Bioenergy with carbon capture and utilization: a review on the potential deployment towards a European circular bioeconomy, Renew. Sustain. Energy Rev. 152 (2021), 111641.

[6] S. Lawson, K. Baamran, K. Newport, F. Rezaei, A.A. Rownaghi, Formulation and processing of dual functional adsorbent/catalyst structured monoliths using an additively manufactured contactor for direct capture/conversion of CO_2 with cogeneration of ethylene, Chem. Eng. J. 431 (2022), 133224.

[7] J. Tian, J. Li, S. Qian, Z. Zhang, S. Wan, S. Wang, J. Lin, Y. Wang, Understanding the origin of selective oxidative dehydrogenation of propane on boron-based catalysts, Appl. Catal. A: Gen. 623 (2021), 118271.

[8] M.A. Sabri, S. Al Jitan, D. Bahamon, L.F. Vega, G. Palmisano, Current and future perspectives on catalytic-based integrated carbon capture and utilization, Sci. Total Environ. 790 (2021), 148081.

[9] S. Sun, H. Sun, P.T. Williams, C. Wu, Recent advances in integrated CO_2 capture and utilization: a review, Sustain. Energy Fuels 5 (2021) 4546–4559.

[10] Z. Lv, C. Qin, S. Chen, D.P. Hanak, C. Wu, Efficient-and-stable CH_4 reforming with integrated CO_2 capture and utilization using Li_4SiO_4 sorbent, Sep. Purif. Technol. 277 (2021), 119476.

[11] S. Molina-Ramírez, M. Cortés-Reyes, C. Herrera, M.A. Larrubia, L.J. Alemany, CO_2-SR cyclic technology: CO_2 storage and in situ regeneration with CH_4 over a new dual function NiBa unsupported catalyst, J. CO_2 Util. 40 (2020), 101201.

[12] H. Sun, J. Wang, J. Zhao, B. Shen, J. Shi, J. Huang, C. Wu, Dual functional catalytic materials of Ni over Ce-modified CaO sorbents for integrated CO_2 capture and conversion, Appl. Catal. B: Environ. 244 (2019) 63–75.

[13] S. Sun, Z. Lv, Y. Qiao, C. Qin, S. Xu, C. Wu, Integrated CO_2 capture and utilization with CaO-alone for high purity syngas production, Carbon Capture Sci. Technol. 1 (2021), 100001.

[14] C. Jeong-Potter, R. Farrauto, Feasibility study of combining direct air capture of CO_2 and methanation at isothermal conditions with dual function materials, Appl. Catal. B: Environ. 282 (2021), 119416.

[15] A. Porta, C.G. Visconti, L. Castoldi, R. Matarrese, C. Jeong-Potter, R. Farrauto, L. Lietti, Ru-Ba synergistic effect in dual functioning materials for cyclic CO_2 capture and methanation, Appl. Catal. B: Environ. 283 (2021), 119654.

[16] A. Porta, R. Matarrese, C.G. Visconti, L. Castoldi, L. Lietti, Storage material effects on the performance of Ru-Based CO_2 capture and methanation dual functioning materials, Ind. Eng. Chem. Res. 60 (2021) 6706–6718.

[17] K. Ghaib, F. Ben-Fares, Power-to-methane: a state-of-the-art review, Renew. Sustain. Energy Rev. 81 (2018) 433–446.

[18] M.S. Duyar, M.A.A. Treviño, R.J. Farrauto, Dual function materials for CO_2 capture and conversion using renewable H_2, Appl. Catal. B: Environ. 169 (2015) 370–376.

[19] A.I. Tsiotsias, N.D. Charisiou, I.V. Yentekakis, M.A. Goula, The role of alkali and alkaline earth metals in the CO_2 methanation reaction and the combined capture and methanation of CO_2, Catalysts 10 (2020) 7.

[20] I.S. Omodolor, H.O. Otor, J.A. Andonegui, B.J. Allen, A. Alba-Rubio, Dual-function materials for CO_2 capture and conversion: a review, Ind. Eng. Chem. Res. 59 (2020) 17612–17631.

[21] P. Melo Bravo, D.P. Debecker, Combining CO_2 capture and catalytic conversion to methane, Waste Dispos. Sustain. Energy 1 (2019) 53–65.

[22] A. Bermejo-López, B. Pereda-Ayo, J.A. González-Marcos, J.R. González-Velasco, Mechanism of the CO_2 storage and in situ hydrogenation to CH_4. Temperature and adsorbent loading effects over Ru-CaO/Al_2O_3 and Ru-Na_2CO_3/Al_2O_3 catalysts, Appl. Catal. B: Environ. 256 (2019), 117845.

[23] S. Cimino, F. Boccia, L. Lisi, Effect of alkali promoters (Li, Na, K) on the performance of Ru/Al_2O_3 catalysts for CO_2 capture and hydrogenation to methane, J. CO_2 Util. 37 (2020) 195–203.

[24] A. Bermejo-López, B. Pereda-Ayo, J.A. González-Marcos, J.R. González-Velasco, Ni loading effects on dual function materials for capture and in-situ conversion of CO_2 to CH_4 using CaO or Na_2CO_3, J. CO_2 Util. 34 (2019) 576–587.

[25] Z. Zhou, N. Sun, B. Wang, Z. Han, S. Cao, D. Hu, T. Zhu, Q. Shen, W. Wei, 2D-layered Ni–MgO–Al_2O_3 nanosheets for integrated capture and methanation of CO_2, ChemSusChem 13 (2020) 360–368.

[26] F. Kosaka, Y. Liu, S. Chen, T. Mochizuki, H. Takagi, A. Urakawa, K. Kuramoto, Enhanced activity of integrated CO_2 capture and reduction to CH_4 under pressurized conditions toward atmospheric CO_2 utilization, ACS Sustain. Chem. Eng. 9 (2021) 3452–3463.

[27] S. Cimino, R. Russo, L. Lisi, Insights into the cyclic CO_2 capture and catalytic methanation over highly performing Li-Ru/Al_2O_3 dual function materials, Chem. Eng. J. 428 (2022), 131275.

[28] A. Bermejo-López, B. Pereda-Ayo, J.A. González-Marcos, J.R. González-Velasco, Alternate cycles of CO_2 storage and in situ hydrogenation to CH_4 on Ni-Na_2CO_3/

Al_2O_3: influence of promoter addition and calcination temperature, Sustain. Energy Fuels 5 (2021) 1194–1210.
[29] M.S. Duyar, S. Wang, M.A. Arellano-Treviño, R.J. Farrauto, CO_2 utilization with a novel dual function material (DFM) for capture and catalytic conversion to synthetic natural gas: an update, J. CO2 Util. 15 (2016) 65–71.
[30] M.A. Arellano-Treviño, Z. He, M.C. Libby, R.J. Farrauto, Catalysts and adsorbents for CO_2 capture and conversion with dual function materials: limitations of Ni-containing DFMs for flue gas applications, J. CO2 Util. 31 (2019) 143–151.
[31] S.B. Jo, J.H. Woo, J.H. Lee, T.Y. Kim, H.I. Kang, S.C. Lee, J.C. Kim, A novel integrated CO_2 capture and direct methanation process using Ni/CaO catal-sorbents, Sustain. Energy Fuels. 4 (2020) 4679–4687.
[32] A. Al-Mamoori, H. Thakkar, X. Li, A.A. Rownaghi, F. Rezaei, Development of potassium- and sodium-promoted CaO adsorbents for CO_2 capture at high temperatures, Ind. Eng. Chem. Res. 56 (2017) 8292–8300.
[33] C.H. Lee, S.W. Choi, H.J. Yoon, H.J. Kwon, H.C. Lee, S.G. Jeon, K.B. Lee, Na_2CO_3-doped CaO-based high-temperature CO_2 sorbent and its sorption kinetics, Chem. Eng. J. 352 (2018) 103–109.
[34] E. Miyazaki, Chemisorption of diatomic molecules (H_2, N_2, CO) on transition d-metals, J. Catal. 65 (1980) 84–94.
[35] Q. Pan, J. Peng, T. Sun, S. Wang, S. Wang, Insight into the reaction route of CO_2 methanation: promotion effect of medium basic sites, Catal. Commun. 45 (2014) 74–78.
[36] A. Lindholm, N.W. Currier, J. Dawody, A. Hidayat, J. Li, A. Yezerets, L. Olsson, The influence of the preparation procedure on the storage and regeneration behavior of Pt and Ba based NO_x storage and reduction catalysts, Appl. Catal. B: Environ. 88 (2009) 240–248.
[37] J. Ashok, Y. Kathiraser, M.L. Ang, S. Kawi, Bi-functional hydrotalcite-derived NiO–CaO–Al_2O_3 catalysts for steam reforming of biomass and/or tar model compound at low steam-to-carbon conditions, Appl. Catal. B: Environ. 173 (2015) 116–128.
[38] T.S. Nguyen, L. Lefferts, K.B. Saisankargupta, K. Seshan, Catalytic conversion of biomass pyrolysis vapours over sodium-based catalyst: a study on the state of sodium on the catalyst, ChemCatChem 7 (2015) 1833–1840.
[39] C.J. Keturakis, F. Ni, M. Spicer, M.G. Beaver, H.S. Caram, I.E. Wachs, Monitoring solid oxide CO_2 capture sorbents in action, ChemSusChem 7 (2014) 3459–3466.
[40] S. Wang, E.T. Schrunk, H. Mahajan, R.J. Farrauto, The role of ruthenium in CO_2 capture and catalytic conversion to fuel by dual function materials (DFM), Catalysts 7 (2017) 3.
[41] A. Efremova, T. Rajkumar, Á. Szamosvölgyi, A. Sápi, K. Baán, I. Szenti, J. Gómez-Pérez, G. Varga, J. Kiss, G. Halasi, Á. Kukovecz, Z. Kónya, Complexity of a Co_3O_4 system under ambient-pressure CO_2 methanation: influence of bulk and surface properties on the catalytic performance, J. Phys. Chem. C 125 (2021) 7130–7141.
[42] A. Efremova, I. Szenti, J. Kiss, Á. Szamosvölgyi, A. Sápi, K. Baán, L. Olivi, G. Varga, Z. Fogarassy, B. Pécz, Á. Kukovecz, Z. Kónya, Nature of the Pt-cobalt-oxide surface interaction and its role in the CO_2 methanation, Appl. Surf. Sci. 571 (2022), 151326.
[43] T.A. Le, T.W. Kim, S.H. Lee, E.D. Park, Effects of Na content in Na/Ni/SiO_2 and Na/Ni/CeO_2 catalysts for CO and CO_2 methanation, Catal. Today 303 (2018) 159–167.
[44] L. Xu, H. Yang, M. Chen, F. Wang, D. Nie, L. Qi, X. Lian, H. Chen, M. Wu, CO_2 methanation over Ca doped ordered mesoporous Ni-Al composite oxide catalysts: the promoting effect of basic modifier, J. CO2 Util. 21 (2017) 200–210.
[45] A. Bermejo-López, B. Pereda-Ayo, J.A. González-Marcos, J.R. González-Velasco, Modeling the CO_2 capture and in situ conversion to CH_4 on dual function Ru-Na_2CO_3/Al_2O_3 catalyst, J. CO_2 Util. 42 (2020), 101351.
[46] A. Bermejo-López, B. Pereda-Ayo, J.A. González-Marcos, J.R. González-Velasco, Simulation-based optimization of cycle timing for CO_2 capture and hydrogenation with dual function catalyst, Catal. Today (2021), https://doi.org/10.1016/j.cattod.2021.08.023.